Volume 1 | Number 1 | Jan 2013 | Pages 1–100

Journal of
Materials Chemistry B

Materials for biology and medicine
www.rsc.org/materialsB

ROYAL SOCIETY
OF CHEMISTRY

ROYAL SOCIETY
OF CHEMISTRY

www.rsc.org/materialsB

Journal of Materials Chemistry B

PAPER

Spontaneous Helical Structure Formation in Laminin Nanofibers

John M. Szymanski[a†] Mengchen Ba,[b†] and Adam W. Feinberg[a,b*]

Laminin is a cross-shaped heterotrimer composed of three polypeptides chains that assembles into an insoluble extracellular matrix (ECM) network as part of the basement membrane, serving a vital role in many processes such as embryonic development, differentiation, and muscle and nerve regeneration. Here we engineered monodisperse laminin nanofibers using a surface-initiated assembly technique in order to investigate how changes in protein composition affect formation and structure of the network. Specifically, we compared laminin 111 with varying degrees of purity and with and without entactin to determine whether these changes alter biophysical properties. All the laminin types were reproducibly patterned as 200 μm long, 20 μm wide nanofibers that were successfuly released during surface-initiated assembly into solution. All nanofibers contracted upon release, and while initial lengths were identical, lengths of released fibers depended on the laminin type. Uniquely, the laminin 111 at high purity (>95%) and without entactin spontaneouly formed helical nanofibers at greater than 90%. Atomic force microscopy revealed that the nanofiber contraction was associated with a change in nanostructure from fibrillar to nodular, suggestive of refolding of laminin molecules into a globular-like conformation. Further, for the high purity laminin that formed helices, the density of the laminin at the edges of the nanofiber was higher than in the middle, providing a possible origin for the differential pre-stress driving the helix formation. Together, these results show that variation in the purity of laminin 111 and presence of entactin can have significant impact on the biophysical properties of the assembled protein networks. This highlights the fact that our understanding of protein assembly and function is still incomplete and that cell-free, in vitro assays can provide unique insights into the ECM.

Introduction

The basement membrane (BM) is a protein dense, sheet-like extracellular matrix (ECM) found at the basal surface of epithelial and endothelial cells and surrounding muscle, fat and Schwann cells. Primary functions of the BM include providing mechanical stability through integrin-mediated adhesion as well as regulating cell differentiation, survival, migration and signaling.[1-3] Laminin and collagen type IV are major components of the BM and together form an interpenetrating network cross-linked together via entactin, perlecan and other molecules.[4] Laminin is of particular interest because it is a cross-shaped heterotrimer composed of α, β, and γ chains that contain domains associated with self-assembly, cell adhesion, growth factor binding and other biological processes.[5-7] There are a number of isoforms for each type of chain, which can combine together in multiple combinations, resulting in over 15 isoforms of the laminin heterotrimer. Each laminin isoform is thought to have unique

biological functionality,[8] with differences attributed to the presence or absence of different functional domains within the protein.[9-11] For example, the laminin LN domain is important for self-assembly,[12, 13] the LE domain in the γ chain has been shown to have specific function, binding entactin,[14] and the LG domains bind cellular receptors and some other ECM component like heparin, sulfatides and other proteins.[6] With evidence that specific laminin isoforms are important in diverse areas from maintaining pluripotency of human pluripotent stem cells in culture[15] to metastatic potential in cancer,[16, 17] improved in vitro models for understanding how laminins assemble and function is or broad interest.

Because laminin is predominantly found polymerized within an insoluble BM, studying it directly requires techniques that enable in vitro formation, analysis and manipulation in the assembled state. The first mechanistic insights into laminin polymerization came from in vitro studies using purified laminin 111 from the Engelbreth-Holm-Swarm (EHS) murine sarcoma. Laminin 111 polymerizes in the presence of calcium ions, which induce a conformational change in the LN domains that allows them to interact.[18] Laminin fragments without one or more short arms do not polymerize and short-arm fragments lacking the LN domains fail to inhibit polymerization.[13] Based on these observations, a three-arm interaction model of laminin assembly was developed,[19] though in vivo data suggests that anchorage to the cell surface is required for recruitment of other components into the

a. Department of Biomedical Engineering, Carnegie Mellon University, Pittsburgh, Pennsylvania 15219, USA.
b. Department of Materials Science and Engineering, Carnegie Mellon University, Pittsburgh, Pennsylvania, 15219, USA. Email: feinberg@andrew.cmu.edu
† These authors contributed equally to this work.
Electronic Supplementary Information (ESI) available: [details of any supplementary information available should be included here]. See DOI: 10.1039/x0xx00000x

Journal of Materials Chemistry B Accepted Manuscript

nascent BM during assembly.[5, 6, 11, 20] This complex polymerization process has made it challenging to study laminin networks in controlled systems in order to study fundamental aspects of assembly, structure and function.

Here we report development of a method to engineer laminin networks with complex topology and composition in a cell-free environment. To do this we use a biomimetic surface-initiated assembly (SIA) process that utilizes protein-surface interactions to drive ECM protein assembly.[21, 22] Originally developed for engineering fibronectin nanofibers, we have recently demonstrated that SIA is also capable of assembling laminin for applications in cell encapsulation and complex surface micropatterning.[23, 24] A unique aspect of the SIA process is that when the assembled laminin is released from the surface, the network will contract due to conformational changes of the constituent protein molecules. In this study, we engineered monodisperse laminin nanofibers in order to investigate the molecular-scale origins of this contraction as a function of the protein composition within the assembled network. We have evaluated three different laminin formulations and assessed differences in fiber formation and morphology. Uniquely, we found that the highest purity laminin produced nanofibers that spontaneously adopted a helical conformation, a phenomenon not previously observed for other laminin and fibronectin nanofibers.[21, 25] Atomic force microscopy (AFM) was then used to investigate the nanoscale architectures of the different laminin nanofiber compositions as an initial step towards understanding the origin of differential stresses within the high purity laminin networks that might drive the helical fiber formation.

## Experimental

Materials and Methods

Preparation of polydimethylsiloxane stamps

Polydimethylsiloxane (PDMS) stamps for microcontact printing consisting of an array of 20 μm wide, 200 μm long rectangles were fabricated according to published methods.[21-23] Briefly, glass wafers were spincoated with SPR 220.3 positive photoresist (Microchem), exposed to UV light through a transparency-based photomask and developed using MF-319 developer (Microchem). Sylgard 2184 PDMS (Dow Corning) was then mixed in a 10:1 base to curing agent ratio, mixed and degassed and then poured on the patterned photoresist and cured at 65°C for 4 hours. PDMS were then cut out and sonicated in a 50% ethanol solution for 45 minutes and dried under a stream of nitrogen.
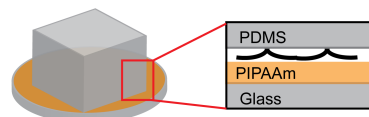
Surface initiated assembly of laminin nanofibers

SIA of laminin nanofibers was performed based on previously published methods.[21-23] Briefly, 25 mm diameter glass coverslips (Thermo Fisher Scientific) were spincoated with 10 wt% solution of PIPAAm (Polysciences) in 1-butanol at 6,000 RPM for 105 seconds. PDMS stamps were then
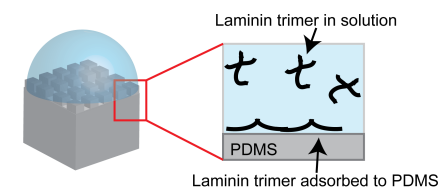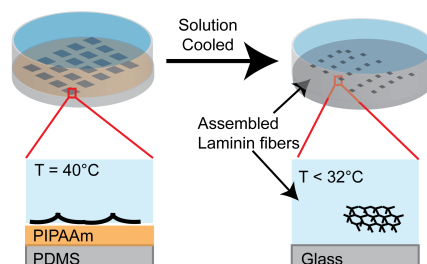

Fig. 1. A schematic of the surface-initiated assembly process. (a) Laminin heterotrimers in their solution conformation were adsorbed onto a hydrophobic PDMS stamp where they obtained a partially unfolded conformation. (b) The laminin trimers were transferred in the unfolded state to a PIPAAm surface via microcontact printing to create an array of patterned nanofibers. (c) The PIPAAm was hydrated at an elevated temperature and allowed to cool below its LCST resulting in the release of assembled laminin nanofibers.

incubated with laminin in sterile DI water at a concentration of 50 μg/mL for 45 min, washed 2 times in DI water to remove excess laminin, and dried under stream of nitrogen (Fig. 1a). The laminin types used all from EHS tumor were (i) >95% pure entactin free laminin 111 (Lam95, Corning® ultrapure laminin, product #354239), (ii) >90% pure entactin free laminin 111 (Lam90, Corning® laminin, product #354232) and (iii) >90% pure laminin 111 and entactin complex (Lam+E, Corning® laminin/entactin, product #354259). The laminin coated PDMS stamps were brought into conformal contact with the PIPAAm coated coverslips for 10 min to create arrays of 200 x 20 μm laminin rectangles on the PIPAAm surface (Fig. 1b). Next, patterned coverslips were placed in a 35 mm petri dish and laminin nanofibers were released by adding 800 μL of 40°C, DI water and allowing it to cool to room temperature, through the lower critical solution temperature of PIPAAm resulting in the dissolution of the PIPAAm (Fig. 1c).

Analysis of laminin nanofiber release and morphology

For 2D analysis, the laminin nanofiber release was recorded optically by phase contrast microscopy and time-lapse imaging at 10x and 1 frame-per-second, using a Photometrics CoolSnap ES digital camera. The same nanofibers were tracked continuously within a field of view and the

contour length of greater than 10 nanofibers per experiment were measured using ImageJ.[26] For helical analysis, the number of ½ turns (180 degree rotation) per nanofiber in solution was counted from the optical phase images. Only helical turns that were clearly stable over >2 minutes were recorded. Helical turns were used rather than pitch because many fibers contained only 0.5 turns and it was difficult to accurately quantify pitch from the low-resolution optical phase images. For 3D analysis, the laminin was labeled with an Alexa Fluor 488 succinimidyl ester fluorescent dye (Life Technologies) per manufacturer's instructions. Samples were then imaged at 63x with a zoom factor of 0.5 using a laser scanning confocal microscope (LSM 700, Zeiss) and post-processed using Imaris 8.0 (Bitplane).

Analysis of nanostructure using atomic force microscopy

Laminin nanofibers were imaged in the pre- and post-release states using AFM (MFP-3D-BIO, Asylum Research) in AC mode in air with AC160TS-R3 cantilevers (Olympus Corporation). For AFM imaging, low resolution scans were first performed with a scan size of 1024x1024 points and lines over a scan area of 16 μm x 32 μm area for the Lam95 fiber pre-release and a scan area of 30 μm x 90 μm for the Lam95 fiber post-release. To resolve the nanostructure, the scan size was kept at 1024x1024 points and lines but the scan area was reduced to 1.5 μm x 1.5 μm and 4.0 μm x 4.0 μm for the Lam95 fibers pre- and post-release, respectively. Measurement of Lam95 nanofiber thickness was performed in

the Igor Pro software environment. Briefly, the AFM height channel was first processed to flat to ensure the background was flat and centered at 0 nm. This was accomplished by applying a mask on the Lam95 nanofiber and subsequently subjecting the non-masked regions to a 1st order flattening. Once the background was appropriately flattened and centered at 0 nm, the thickness of the nanofibers could be measured.

Circular Dichroism Spectroscopy of Laminin in Solution Form

The far-UV circular dichroism (CD) spectra of Lam95, Lam90, and Lam+E in solution form were recorded using a Jasco J-810 spectropolarimeter (Jasco, Inc.). To recapitulate the experimental conditions used for SIA of the nanofibers, each laminin type was diluted to a concentration of 50 μg/mL in DI water and measurements were recorded at room temperature. The spectra for each laminin type are the average of 3 independent experiments with 5 accumulations per experiment. The data are reported as mean residue ellipticity, with a mean residue molecular weight of 110 g/mol.

Results and discussion

Surface-initiated assembly produces monodisperse laminin nanofibers

Laminin nanofibers were engineered using SIA with initial patterned dimensions of 200 μm in length and 20 μm in width (Fig. 1). Three different sources of laminin 111 were used to
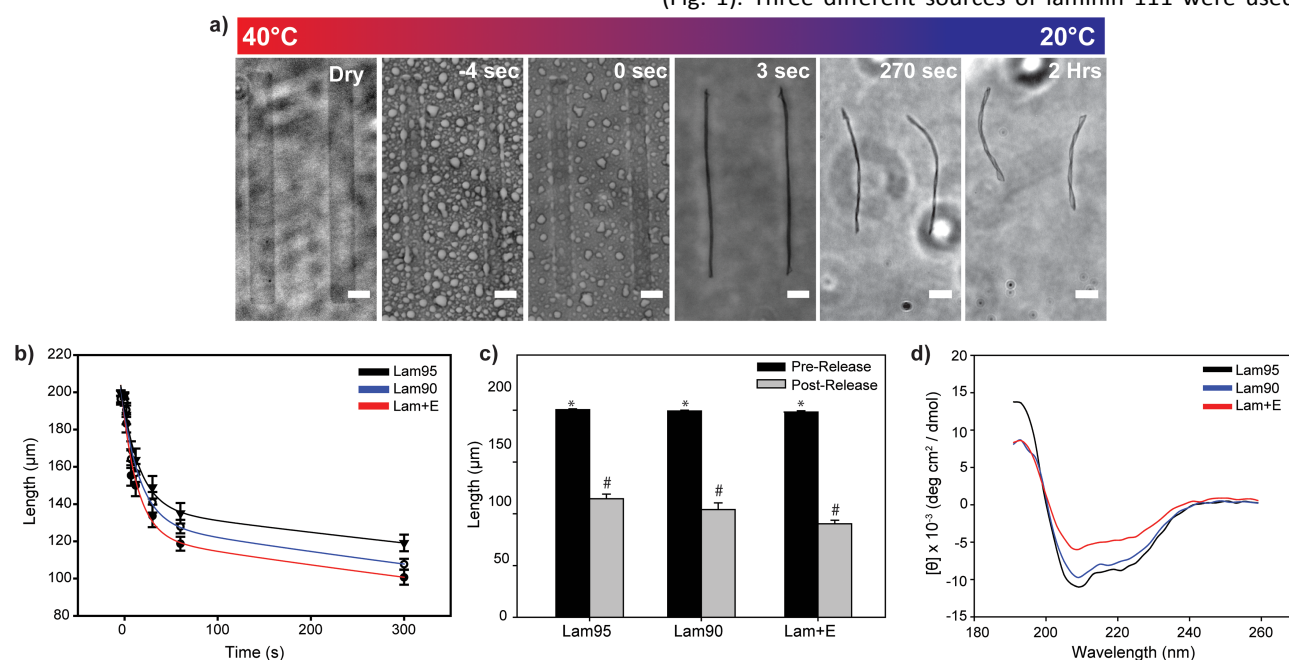
Fig. 2. Measuring the dynamic changes in laminin nanofiber length during the release process. (a) A time-lapse sequence of laminin nanofibers released in distilled water. The times are relative to the initiation of the release from PIPAAm. (b) The contour length as a function of time after release was fit to a double exponential curve (r^2 = 0.98, 0.97, 0.97 for Lam95, Lam90, and Lam+E, respectively). (c) The contour length of the different laminin types was measured in the as-patterned, pre-release state and again after the nanofibers were released and allowed to fully contract in solution. (d) The far-UV CD spectra of the different laminin types in solution, diluted to 50 mg/mL in DI water. Scale bars in (a) are 20 μm. Error bars in (b) and (c) are standard deviation. A two-way ANOVA with a Tukey's pairwise comparison was used to assess differences in laminin nanofiber length between pre- and post-release states and whether there were differences in the different laminin types. * Indicates the pre-release nanofiber length was statistically significant from the post-release nanofiber length, P<0.05, and # indicates statistically significant differences between the post-release laminin length of the different types, P<0.05.

This journal is © The Royal Society of Chemistry 20xx

*J. Mater. Chem. B*, 2015, **00**, 1-3 | **3**

assess whether differences in the purity of the laminin and the presence of entactin affected fiber formation. These were 95% pure laminin (Lam95), 90% pure laminin (Lam90) and 90% pure laminin with entactin (Lam+E) in an equimolar ratio. As part of the SIA process, each of the laminin types in solution was first adsorbed on the surface of a polydimethylsiloxane (PDMS) stamp (Fig. 1a). Next, the PDMS stamp was used to microcontact print the laminin onto a poly N-isopropylacrylamide (PIPAAm) surface (Fig. 1b). Finally, the PIPAAm with patterned protein was submerged in a 40°C DI water and cooled to 22°C, thermally triggering swelling and dissolution of the PIPAAm layer and release of assembled laminin nanofibers (Fig. 1c).

Brightfield phase imaging enabled visualization of the release process in real time and analysis of nanofiber structure. During the SIA process the PIPAAm layer swells and dissolves, releasing the laminin nanofibers into solution (Fig. 2a and Movie 1). Even though the PIPAAm is swelling during this process, the patterned laminin nanofibers actually contract, decreasing in both length and width. Tracking the nanofibers during release revealed a rapid contraction rate upon initial PIPAAm dissolution followed by a slower contraction rate once free floating in solution (Fig. 2b). The release profiles were similar for each of the laminin types, which was expected given the similar compositions, but there were still statistically significant differences. In the initial micropatterned state on the PIPAAm all laminin types had the same fiber dimensions (Fig. 2c). However, after release into solution there were statistically significant differences in the nanofiber length between each laminin type, with Lam95 > Lam90 > Lam+E (Fig. 2c). While the data shows that the nanofibers with less laminin contract more, it was not clear what the mechanism might be that was causing this.

To investigate whether differences in secondary protein structure might have led to the observed differences in nanofiber length, we measured the far-UV CD spectra of Lam95, Lam90, and Lam+E in their trimeric, solution form (Fig. 2d). The CD spectra of the laminin types all contained a minimum at 208 nm and had a shoulder at 220 nm, in agreement with the previously reported CD spectrum of laminin.[27-29] These spectra confirmed that the laminin types all had beta sheet and alpha helix secondary structure. However, while the spectra had a similar shape, the amplitude of the mean residue ellipticity at 208 nm and 220 nm was greatest for Lam95 followed by Lam90 and Lam+E, respectively. This tracks with the amount of laminin in the different laminin types, of >95% (Lam95), >90% (Lam90) and >45% (Lam+E based on equimolar ratio with entactin). This also suggested that the Lam95 (in solution) had the greatest of amount of alpha helix and beta sheet secondary structure as a function of total protein mass.

Laminin nanofibers adopt unique post-release morphologies

Next, we examined the nanofiber structure in solution to determine if the laminin type affected overall morphology.
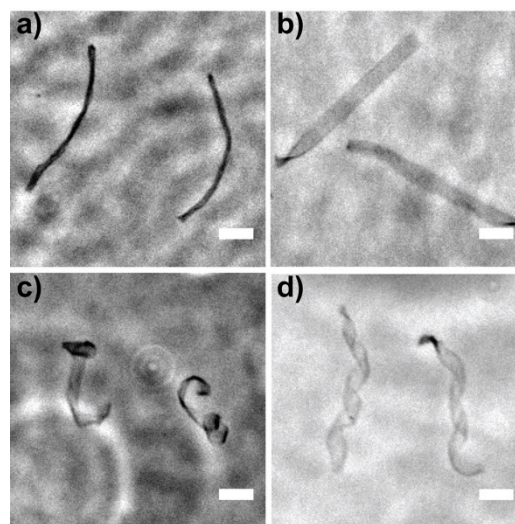
Fig 3. Laminin nanofibers adopt unique post-release morphologies. Lam90 and Lam+E typically formed (a) compacted, linear nanofibers. In some cases, they formed (b) linear ribbon-like fibers due to adhesion to the coverslips or (c) tightly coiled fibers, though this was infrequent and potentially due to defects in the microcontact printing. (d) Lam95 nanofibers formed helical structures, which was unique to Lam95. Scale bars are 20 μm.
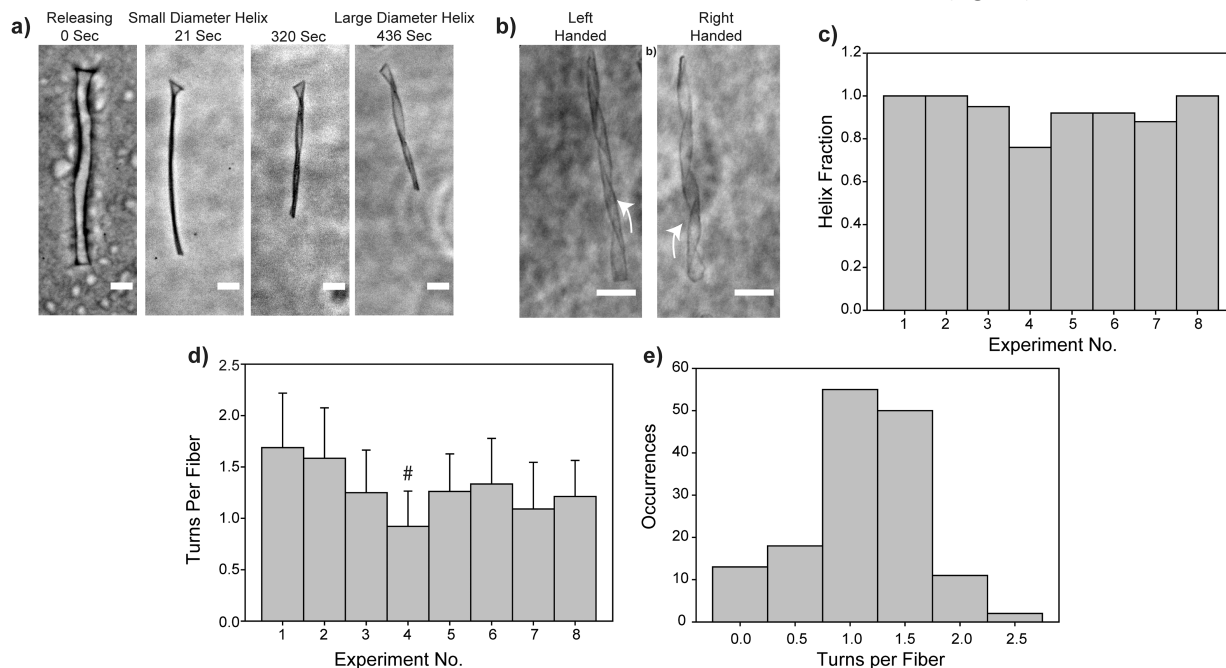
Previous studies using fibronectin showed that SIA creates nanofibers with compact and linear morphologies.[21, 25] This is what we expected for laminin nanofibers, but the resulting fiber morphologies were more varied and depended on laminin type. First, laminin nanofibers were observed in a compacted, linear morphology (Fig. 3a), similar to that previously reported for fibronectin nanofibers. This was typically observed for Lam90 and Lam+E. Second, some nanofibers were observed to essentially unfold into linear ribbon-like fibers (Fig. 3b). It was determined that these nanofibers were partially or entirely adsorbed back onto the surface of the coverslip, and would typically occur after nanofibers were allowed to sit in solution for many hours. Third, some nanofibers were tightly coiled or folded up on themselves in solution (Fig. 3c). This was relatively infrequent, and was thought to be due to defects in the microcontact printing. Finally, some laminin nanofibers were found to adopt a helical conformation in solution (Fig. 3d). This was unique and had not been previously reported before for SIA of any type of ECM protein nanofiber. Importantly, this was only observed for the Lam95 and not the other laminin types. Formation of a helix suggested that there was a pre-stress in the nanofibers that had some degree of spatial anisotropy and that only occurred for the highest purity laminin composition.

Laminin nanofibers spontaneously form helical 3D structures

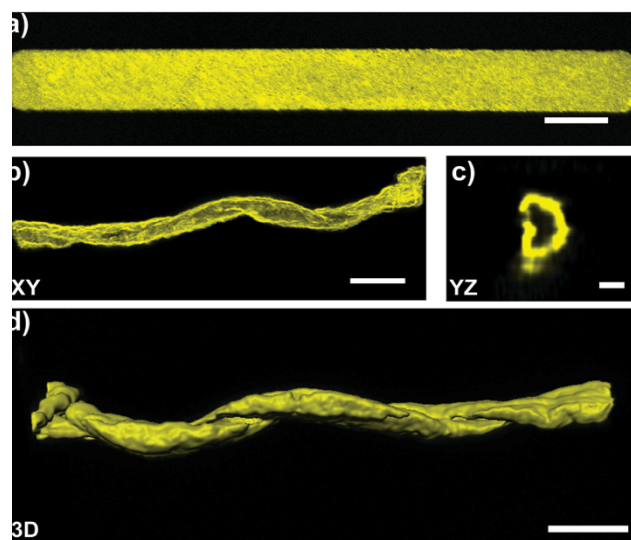The formation of the helical Lam95 nanofibers was unique and we next investigated this morphology in greater detail. First, the helical structure was inferred to be in 3D, but this could not be confirmed directly from the brightfield phase imaging used to observe the fibers in 2D. To address this, the

4 | *J. Mater. Chem. B*, 2015, **00**, 1-3

This journal is © The Royal Society of Chemistry 20xx

Lam95 was fluorescently labeled and then imaged using the confocal microscope. In the patterned, pre-release state the Lam95 nanofiber had the same rectangular shape as observed under phase contrast (Fig. 2a) and was clearly 2D (Fig. 4a). However, in the released state the laminin nanofibers had a clearly defined helical morphology in 3D that could be resolved by the confocal microscope. The XY projection of the Lam95 nanofiber shows the basic helical structure with ~2 complete turns along the fiber length (Fig. 4b). The YZ projection of the same Lam95 nanofiber clearly shows that a true helix is formed with an interior diameter in the range of 2 to 5 μm (Fig. 4c). The helical morphology was best viewed by creating a 3D rendering of the confocal image, where the turning of the helix in 3D space could be easily visualized (Fig. 4d and Movie 2).

To gain insight into the formation of the helical morphology, we tracked a representative nanofiber at high resolution during the release process. Initially the nanofiber had the patterned dimensions, but as soon as the underlying PIPAAm began to dissolve the nanofiber began to release and contract, and by 21 seconds had fully contracted (Fig. 5a). In this state it was difficult to tell if a helix had even formed, but over the next 5 min the nanofiber morphology slowly changed such that the diameter of the helix increased and the helical morphology was readily observed. These results confirm that the helical morphology for the Lam95 occurred at the initial, rapid release from the PIPAAm surface, but also shows that slower morphological change occurred as the nanofibers helical diameter increased.

Fig. 4. Lam95 adopts a 3D helical morphology post-release. (a) Lam95 nanofiber as patterned on PIPAAm, pre-release. (b) XY maximum intensity projection of a Lam95 nanofiber post-release. (c) A YZ slice from the nanofiber in (b) indicates the formation of a helix with an interior diameter in the range of 2 to 5 μm. (d) A 3D rendering of the nanofiber in (b). Scale bars are (a) 20 μm, (b) and (d) 10 μm and (c) 2 μm.

Finally, we analyzed the fraction of Lam95 nanofibers that formed helices and the number of helical turns per nanofiber to understand how repeatable this phenomenon was. Analysis of the helix morphology showed that both left- and right-handed helices were formed (Fig. 5b). We did not observe any
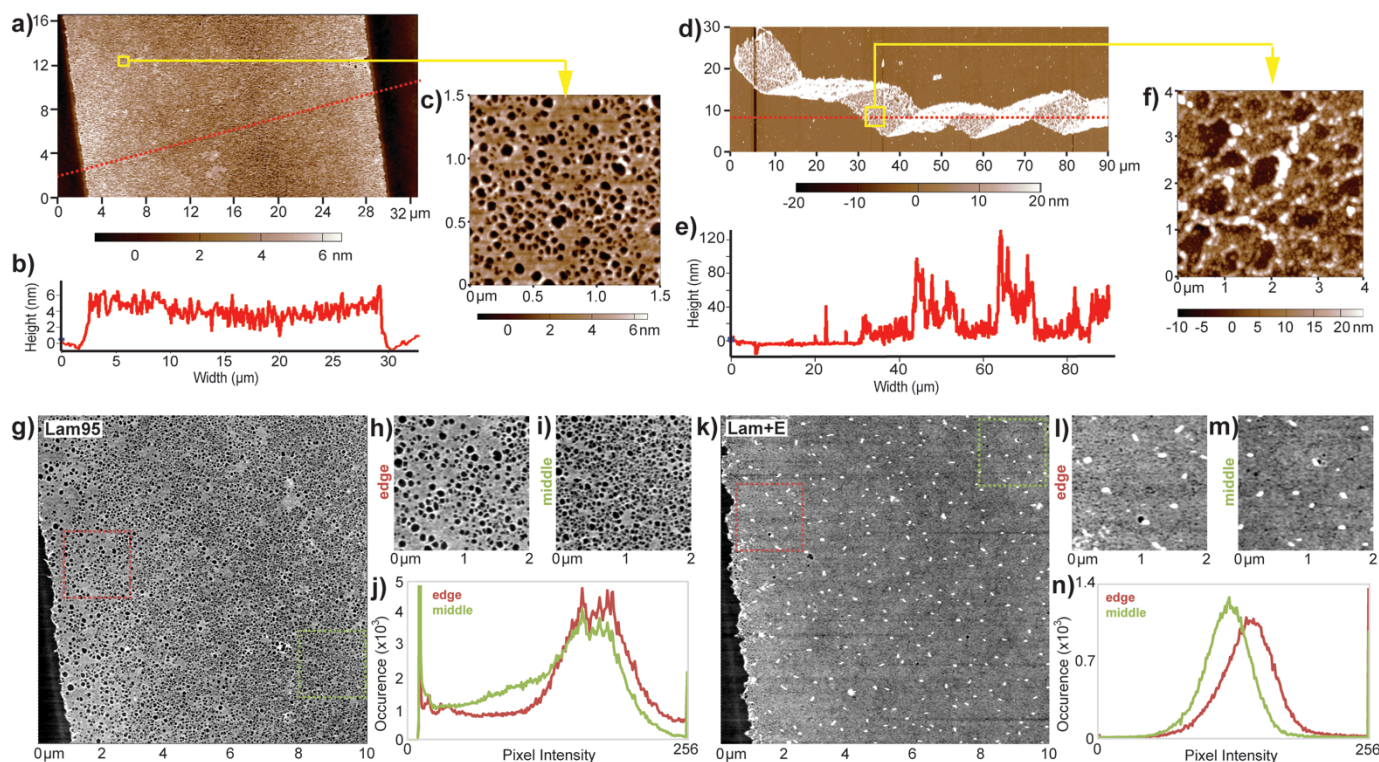

Fig. 5. Quantification of Lam95 helix formation. (a) A time-lapse sequence of a single Lam95 nanofiber during the release process. (b) Representative examples of Lam95 helices immediately after nanofiber formation showing presence of left- and right-handed helices, with no observed preference for either morphology. (c) Quantification of the fraction of Lam95 nanofibers that formed helices through 8 independent experiments. (d) The average number of turns per Lam95 nanofiber for each experiment. A one-way ANOVA was performed with a Dunn's pairwise comparison. # Indicates a statistically significant different than experiment 1 with a $P<0.05$. (e) Histogram illustrating the number of turns per fiber for the fibers measured across all of the independent experiments. Scales bars are 20 μm.

This journal is © The Royal Society of Chemistry 20xx

J. Mater. Chem. B, 2015, **00**, 1-3 | **5**

Fig 6. Nanostructure of laminin nanofibers analyzed by AFM. (a) A representative Lam95 nanofiber pre-release scanned using AFM such that the entire width of a fiber was visible. (b) A cross-sectional profile of the fiber (red dotted line in (a)). (c) A high resolution AFM scan of the Lam95 fiber (yellow box in (a)) showing a fibrillar structure with holes. (d) A representative Lam95 nanofiber post-release in a helical conformation using AFM such that most of the fiber was visible. (e) A cross-sectional profile of the fiber (red dotted line in (d)) through single-layer and multi-layer regions. (f) A high resolution AFM scan of the fiber (yellow box in (d)) showing a nodular network. (g) A representative scan from the edge to middle of a Lam95 nanofiber to highlight the differences in nanostructure between the (h) edge and (i) middle regions. (j) A histogram quantifying pixel intensity between the edge (red) and middle (green) confirms the higher density of holes in the middle. (k) A representative scan from the edge to middle of a Lam+E nanofiber to highlight the similar nanostructure between the (l) edge and (m) middle regions. (n) A histogram quantifying pixel intensity between the edge (red) and middle (green) confirms that the structure is similar across the fiber width.

preference for either morphology, with an approximately equal number of each handedness. Through 8 independent experiments using Lam95, 75-100% of the nanofibers formed helices, for an average of 93 ± 8% (Fig. 5c). We defined a full turn of the helix to be 360° and counted the number of half turns per nanofiber because these could be easily identified in the phase images. Results show that across 8 experiments the average number of turns varied from 1 to 1.5 over the nanofibers length (Fig. 5d). While there was a statistically significant difference between two of the eight experiments, we considered this to be a consistent and repeatable result. Combining the data from all eight experiments into a single histogram showed that the majority of the nanofibers fell within this range (Fig. 5e).

Laminin nanostructure changes during fiber formation

To gain further insight into how the different types of laminin might be impacting nanoscale structure, and thus fiber morphology, we performed AFM analysis of the nanofibers in the pre- and post-release states. In the pre-released state on the PIPAAm surface the patterned laminin had the appearance of a uniform layer of protein (Fig. 6a). The image shown is for Lam95, but the appearance over a 30 μm scan size was similar for Lam90 and Lam+E. A cross-sectional profile showed that the laminin was on the order of 4 to 5 nm thick (Fig. 6b), specifically 4.43 ± 0.52 nm thick for Lam95 and 4.12 ± 0.59 nm thick for Lam+E, with no statistical difference between laminin types. Laminin 111 is known to have a diameter of ~20 nm in solution,[30] thus the microcontact printed laminin on the PIPAAm surface is clearly in a partially denatured state. This unfolded thickness is consistent with previous results for fibronectin on PIPAAm,[21, 22, 25] and previous AFM studies of laminin trimmers adsorbed to surfaces have also shown that the molecules can unfold.[31] Based on these results, we estimated that the laminin nanofibers were only a few molecules thick at most.

At higher resolution AFM imaging revealed that the nanostructure consisted of a constant thickness layer with multiple holes in it, resembling a fibrillar mesh (Fig. 6c). This general structure was observed for all laminin types, and appeared to be isotropic. These types of holes are similar to those previously reported by AFM in assembled laminin

6 | *J. Mater. Chem. B*, 2015, **00**, 1-3

This journal is © The Royal Society of Chemistry 20xx

networks,[32] although the size range is larger suggesting this is not a network assembled via the three-arm interaction model.[19] The length of the 'struts' within the network were ~55 nm, similar to the arms of the laminin heterotrimers, which have three short arms in the range of 35 to 50 nm in length.[19] Thus, these could be laminin arms coupled together, but further validation is needed to confirm this.

After release of the laminin nanofibers from the PIPAAm the contraction in length and width was accompanied by an increase in thickness. An AFM image of a Lam95 nanofiber with a helical morphology that was adsorbed back onto a glass coverslip for analysis clearly demonstrated the collapsed morphology (Fig. 6d). Note that the number of helical turns per fiber was typically easier to observe by AFM when dried on the surface than by optical phase microscopy in solution, which in this case clearly showed 3 full turns. A cross-sectional profile showed that the Lam95 was 15.31 $\pm$ 4.97 nm thick in the regions that were one layer thick, and at least 2 times thicker in areas where multiple layers overlapped (Fig. 6e). At higher resolution AFM imaging revealed that the nanostructure consisted of a thicker layer that lacked the fibrillar mesh architecture with small struts seen pre-release (Fig. 6c) and instead appeared to have small nodules present (Fig. 6f). The presence of these nodules in combination with the increased thickness suggests that the contraction observed in the nanofibers during release might be due to refolding of the laminin trimmers into more of a globular, solution-like conformation. Note that the size of these nodules at >50 nm is much larger than the beta sheet folded domains within the laminin molecule[33] and similar in size to the full trimeric molecule.[29] A similar transition from a fibrillar to nodule morphology has been observed in fibronectin nanofibers and was contributed to tertiary structure from partial refolding of dimers into a globular state.[22] Importantly, both the pre- and post-release nanofibers had an overall nanoscale structure that appeared to be isotropic. This suggests that the helical morphology was not due to a directional bias in the assembly of the constituent laminin molecules.

Potential mechanisms for helix formation in laminin nanofibers

Formation of the helical nanofiber morphology by the Lam95 strongly suggested that there was anisotropic pre-stress in the nanofiber driving this process. The finding that this was due to pre-stress is based on the fact that the helical morphology occurred within seconds of PIPAAm dissolution (Fig. 5a and Movie 1) and thus unlikely to be due to new intermolecular interactions between laminin molecules in the released fiber, which would occur over a longer time scale. Further, the presence of fibrillar structures in the pre-release nanofiber (Fig. 6c) were replaced by a nodular structures and increased thickness post-release (Fig. 6f), suggesting refolding of laminin molecules into a more globular state.

The helical morphology could be caused by two different potential mechanisms, (i) a directional anisotropy of molecular assembly within the nanofiber or (ii) a differential pre-stress within the nanofiber due to another reason.[34-36] We ruled out directional anisotropy of molecular assembly of the laminin molecules based on the isotropy observed in the higher-resolution AFM scans (Fig. 6c), which was consistent with previous experience for fibronectin nanofibers.[22] Similarly, the helices formed with both left- and right-handedness, suggesting there was no preferential direction of nanoscale organization (Fig. 5b). Another mechanism could be formation of a bilayer film with different pre-stress in each layer.[34, 36] While this is certainly possible, it was unlikely given the thickness of ~4 nm of the pre-release nanofibers (Fig. 6b), which was on the order of 1 to 3 molecules thick. However, another possibility was a differential pre-stress across the width of the nanofiber.[35]

We next used the AFM to determine whether the Lam95 had different nanostructure across the width of the nanofiber compared this to Lam+E. We imaged a pre-release Lam95 nanofiber from the edge to middle (Fig. 6g) and directly compared sub-regions from the edge (Fig. 6h) and the middle (Fig. 6i). A histogram of pixel intensity for each region showed clearly that the middle regions had more holes (lower pixel intensity values), and thus less laminin than the edge regions (Fig. 6j). For comparison, we imaged a pre-release Lam+E nanofiber from the edge to middle (Fig. 6k) and also directly compared sub-regions from the edge (Fig. 6l) and the middle (Fig. 6m). A histogram of pixel intensity for each region showed that for Lam+E the edge and middle regions appeared about the same, with no more holes in one versus the other (Fig. 6j). This difference in laminin density between edge and middle for Lam95 is a potential source or differential pre-stress that could cause formation of a helical morphology.[35]

This is an important insight, however questions remain about how the helix forms. First, why is there a difference in laminin density across the width of the laminin nanofiber and only for Lam95? It is possible this is due to a difference in adsorption of Lam95 onto the PDMS stamp used for microcontact printing, which has been reported in other systems.[37] Or is it due to a difference in transfer of Lam95 from the PDMS stamp to the PIPAAm surface. However, additional studies will be required to determine if either of these occur, and if so why. A second question is which region, edge or middle, is under higher pre-stress? On the edge there is more laminin present and thus more molecules that are potentially refolding from a fibrillar to globular state during release. Conversely, in the middle there are more holes and potentially more space for molecules to refold and pack together during release. Unfortunately, AFM of the released Lam95 nanofiber (Fig. 6e and 6f) did not reveal any clear structural differences. The CD data indicated that the Lam95 molecules in solution, prior to SIA, had the greatest alpha helix and beta sheet content (Fig. 2D). However, differences in CD spectra between Lam95 and Lam90 were quite small, and it is unclear whether this difference would have any significant impact on nanofiber morphology. Thus, while we have identified a potential mechanism for helix formation, why specifically this occurs for Lam95 as opposed to other laminin types requires further study.

This journal is © The Royal Society of Chemistry 20xx

J. Mater. Chem. B, 2015, **00**, 1-3 | **7**

Conclusions

Here we have engineered monodisperse laminin nanofibers to study how changes in protein purity and composition affect fiber formation and structure. Results show that Lam95, Lam90 and Lam+E nanofibers formed via a similar SIA process. However, there were statistically significant differences in nanofiber lengths post-release, suggesting differences in the way the proteins were behaving. Because Lam95 formed a unique helical nanofiber morphology, we focused our attention on analyzing this fiber type in more detail. Confocal imaging validated that the helix was truly 3D with an internal diameter of 2-5 μm and multiple experiments confirmed that the process was highly repeatable, with greater than 90% of nanofibers forming helices. AFM analysis suggested that the pre-stress in the nanofibers driving contraction from pre-release to post-release state was refolding of fibrillar laminin molecules into a more globular state. Further, for Lam95 there appeared to be a higher density of laminin at the edges of the fiber than in the middle region, serving as a potential mechanism for differential pre-stress within the nanofiber and causing the helix formation. Together, these results showed that even for similar laminin 111 compositions, varying only in purity and presence or absence of entactin, there could be significant differences in the biophysical properties of the assembled protein networks. This is an important insight, and highlights the fact that our understanding of ECM protein assembly and function is still incomplete. While our system is limited in biological relevance because we use purified proteins, future studies will examine how these systems assemble when varying composition to better reflect that in the native BM. We also plan to further investigate mechanisms of laminin assembly as function of laminin type and understand the impact this has on biomechanical properties and cell adhesion and behavior.
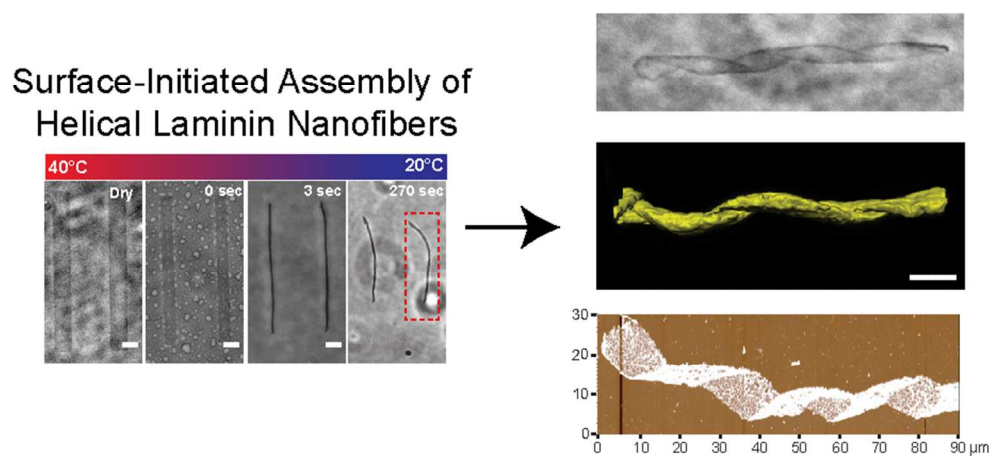
Acknowledgements

Notes and references

1. T. Sasaki, R. Fassler and E. Hohenester, *Journal of Cell Biology*, 2004, **164**, 959-963.
2. B. Geiger, A. Bershadsky, R. Pankov and K. M. Yamada, *Nat Rev Mol Cell Biol*, 2001, **2**, 793-805.
3. V. Vogel and M. Sheetz, *Nat Rev Mol Cell Biol*, 2006, **7**, 265-275.
4. R. Timpl and J. C. Brown, *Bioessays*, 1996, **18**, 123-132.
5. K. K. McKee, D. Harrison, S. Capizzi and P. D. Yurchenco, *Journal Of Biological Chemistry*, 2007, **282**, 21437-21447.
6. R. Timpl, D. Tisi, J. F. Talts, Z. Andac, T. Sasaki and E. Hohenester, *Matrix Biology*, 2000, **19**, 309-317.
7. M. Aumailley, L. Bruckner-Tuderman, W. G. Carter, R. Deutzmann, D. Edgar, P. Ekblom, J. Engel, E. Engvall, E. Hohenester, J. C. R. Jones, H. K. Kleinman, M. P. Marinkovich, G. R. Martin, U. Mayer, G. Meneguzzi, J. H. Miner, M. Miyazaki, M. Patarroyo, M. Paulsson, V. Quaranta, J. R. Sanes, T. Sasaki, K. Sekiguchi, L. M. Sorokin, J. F. Talts, K. Tryggvason, J. Uitto, I. Virtanen, K. von der Mark, U. M. Wewer, Y. Yamada and P. D. Yurchenco, *Matrix Biology*, 2005, **24**, 326-332.
8. N. M. Nguyen and R. M. Senior, *Developmental Biology*, 2006, **294**, 271-279.
9. M. C. Ryan, A. M. Christiano, E. Engvall, U. M. Wewer and R. E. Burgeson, *Matrix Biology*, 1996, **15**, 369-381.
10. P. Tunggal, N. Smyth, M. Paulsson and M. C. Ott, *Microscopy Research and Technique*, 2000, **51**, 214-227.
11. M. Durbeej, *Cell and Tissue Research*, 2010, **339**, 259-268.
12. A. Purvis and E. Hohenester, *Journal of Biological Chemistry*, 2012, **287**, 44270-44277.
13. J. C. Schittny and P. D. Yurchenco, *Journal of Cell Biology*, 1990, **110**, 825-832.
14. M. S. P. Ho, K. Bose, S. Mokkapati, R. Nischt and N. Smyth, *Microscopy Research and Technique*, 2008, **71**, 387-395.
15. S. Rodin, L. Antonsson, O. Hovatta and K. Tryggvason, *Nature Protocols*, 2014, **9**, 2354-2368.
16. C. Pyke, S. Sale, E. Ralfkiaer, J. Romer, K. Dano and K. Tryggvason, *Cancer Research*, 1995, **55**, 4132-4139.
17. Y. Kikkawa, K. Hozumi, F. Katagiri, M. Nomizu, H. K. Kleinman and J. E. Koblinski, *Cell Adhesion & Migration*, 2013, **7**, 150-159.
18. P. D. Yurchenco, E. C. Tsilibary, A. S. Charonis and H. Furthmayr, *Journal of Biological Chemistry*, 1985, **260**, 7636-7644.
19. P. D. Yurchenco and Y. S. Cheng, *Journal of Biological Chemistry*, 1993, **268**, 17286-17299.
20. E. Hohenester and P. D. Yurchenco, *Cell Adhesion & Migration*, 2013, **7**, 56-63.
21. J. M. Szymanski, Q. Jallerat and A. W. Feinberg, *Journal of Visualized Experiments*, 2014, e51176.
22. A. W. Feinberg and K. K. Parker, *Nano Letters*, 2010, **10**, 2184-2191.
23. Y. Sun, Q. Jallerat, J. M. Szymanski and A. W. Feinberg, *Nature Methods*, 2015, **12**, 134-136.
24. R. N. Palchesko, J. M. Szymanski, A. Sahu and A. W. Feinberg, *Cellular and Molecular Bioengineering*, 2014, **7**, 355-368.
25. L. F. Deravi, T. Su, J. A. Paten, J. W. Ruberti, K. Bertoldi and K. K. Parker, *Nano Letters*, 2012, **12**, 5587-5592.
26. C. A. Schneider, W. S. Rasband and K. W. Eliceiri, *Nature Methods*, 2012, **9**, 671–675.
27. U. Ott, E. Odermatt, J. Engel, H. Furthmayr and R. Timpl, *European Journal of Biochemistry*, 1982, **123**, 63-72.
28. J. W. Dean, S. Chandrasekaran and M. L. Tanzer, *Journal of Biological Chemistry*, 1990, **265**, 12553-12562.
29. M. Paulsson, M. Aumailley, R. Deutzmann, R. Timpl, K. Beck and J. Engel, *European Journal of Biochemistry*, 1987, **166**, 11-19.

8 | *J. Mater. Chem. B*, 2015, **00**, 1-3

This journal is © The Royal Society of Chemistry 20xx

30. K. Onuma and N. Kanzaki, *The Journal of Physical Chemistry B*, 2003, **107**, 11799-11804.
31. C. H. Chen, D. O. Clegg and H. G. Hansma, *Biochemistry*, 1998, **37**, 8262-8267.
32. C. Hochman-Mendez, M. Cantini, D. Moratal, M. Salmeron-Sanchez and T. Coelho-Sampaio, *PLoS ONE*, 2014, **9**, e109388.
33. T. R. Patel, G. A. Morris, D. Zwolanek, D. R. Keene, J. Li, S. E. Harding, M. Koch and J. Stetefeld, *Matrix Biology*, 2010, **29**, 565-572.
34. Z. Chen, C. Majidi, D. J. Srolovitz and M. Haataja, *Applied Physics Letters*, 2011, **98**.
35. J. S. Huang, J. Liu, B. Kroll, K. Bertoldi and D. R. Clarke, *Soft Matter*, 2012, **8**, 6291-6300.
36. Y. V. Zastavker, N. Asherie, A. Lomakin, J. Pande, J. M. Donovan, J. M. Schnur and G. B. Benedek, *Proceedings of the National Academy of Sciences of the United States of America*, 1999, **96**, 7883-7887.
37. G. Hodgkinson and V. Hlady, *Journal of adhesion science and technology*, 2008, **19**, 235-255.

This journal is © The Royal Society of Chemistry 20xx

J. Mater. Chem. B, 2015, **00**, 1-3 | **9**

Please do not adjust margins

Surface-initiated assembly is used to engineer laminin nanofibers that spontaneously adopt a helical conformation.
79x37mm (300 x 300 DPI)